Supplement: Vertical responses of urban heat islands to heatwaves and their local climate zones dependence: a case study of Guangzhou, China

Fu Luo[1], Yuanjian Yang[1], Ting Sun[2], Zuofang Zheng[3], Xueyan Bi[4], Guoyu Ren[5], and Simone Lolli[6]

[1]Collaborative Innovation Centre on Forecast and Evaluation of Meteorological Disasters, School of Atmospheric Physics, Nanjing University of Information Science and Technology, Nanjing, China
[2]Department of Risk and Disaster Reduction, University College London, London, UK
[3]Institute of Urban Meteorology, China Meteorological Administration, Beijing, China
[4]Institute of Tropical and Marine Meteorology, Guangzhou, China
[5]Department of Atmospheric Science, School of Environmental Studies, China University of Geosciences, Wuhan, China
[6]CNR-IMAA, Contrada S. Loja, 85050 Tito Scalo (PZ), Italy

Correspondence: Yuanjian Yang (yyj1985@nuist.edu.cn)

Supplement S1: Supplementary results

Supplement S2: Results for HW2

Supplement S3: Radiosonde profile evaluation

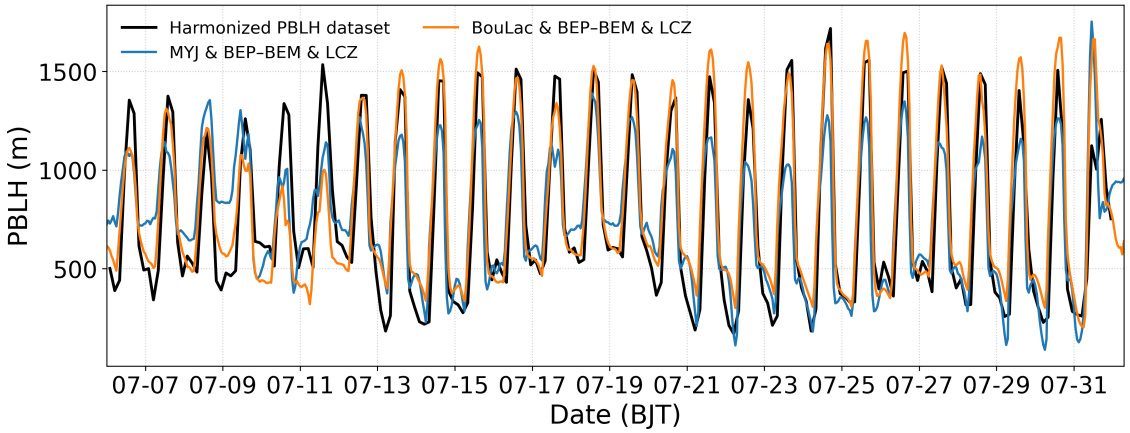

Figure S1. Comparison of the simulated PBLH from the MYJ (blue) and BouLac (orange) planetary boundary layer schemes against the harmonised PBLH dataset of Guo et al. (2022) over the D03 reference area between 6 and 31 July 2020.

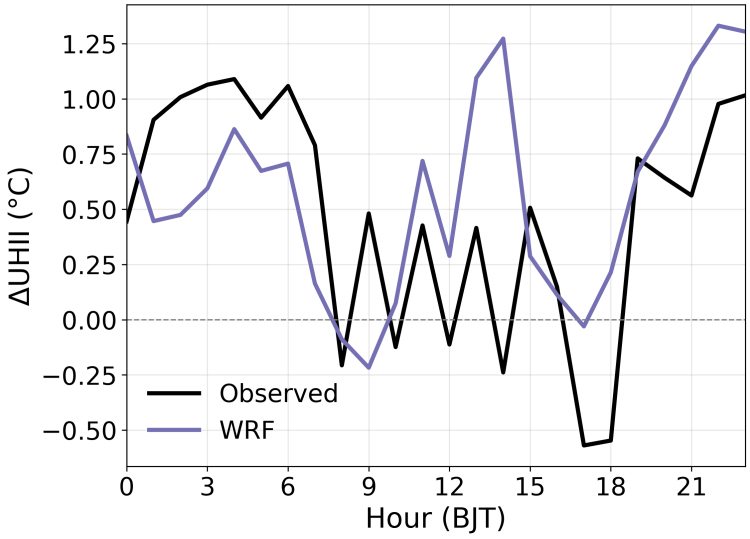

Figure S2. Comparison of simulated and observed ΔCUHII (HW - NHW) over the CUR, showing the averaged diurnal cycle over the analysis periods.

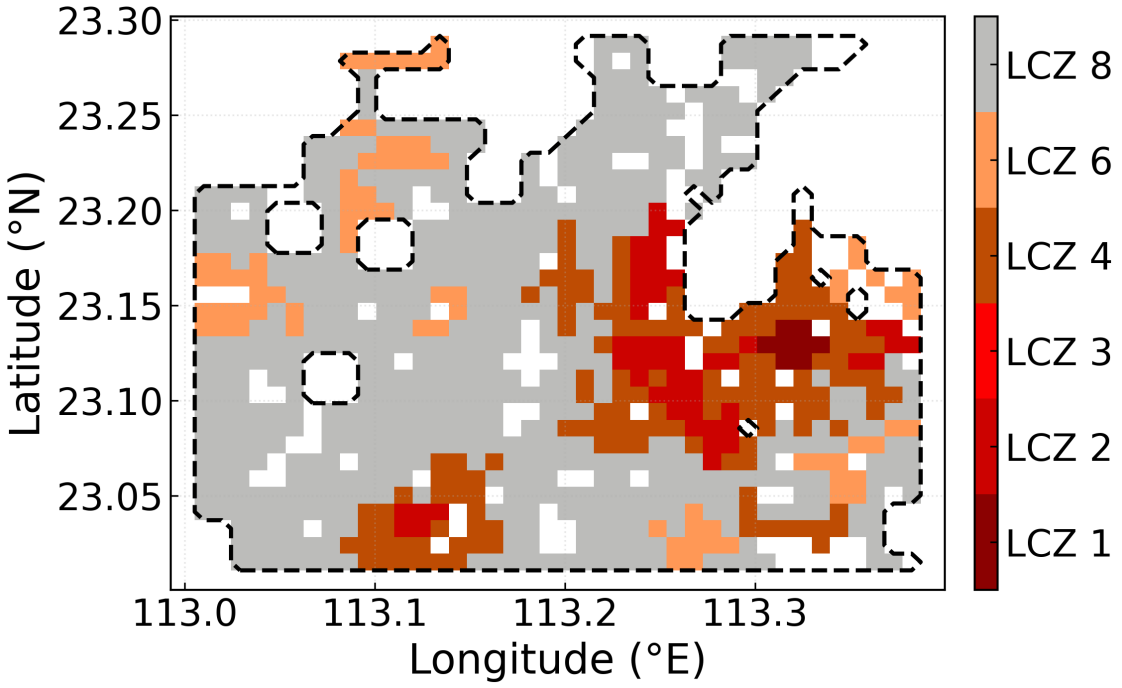

Figure S3. Spatial distribution within the CUR of the LCZ samples used in the analysis, after the connectivity-based screening described in Sect. 2.4. Coloured grid cells denote LCZ 1, 2, 4, 6, and 8 retained for the analysis.

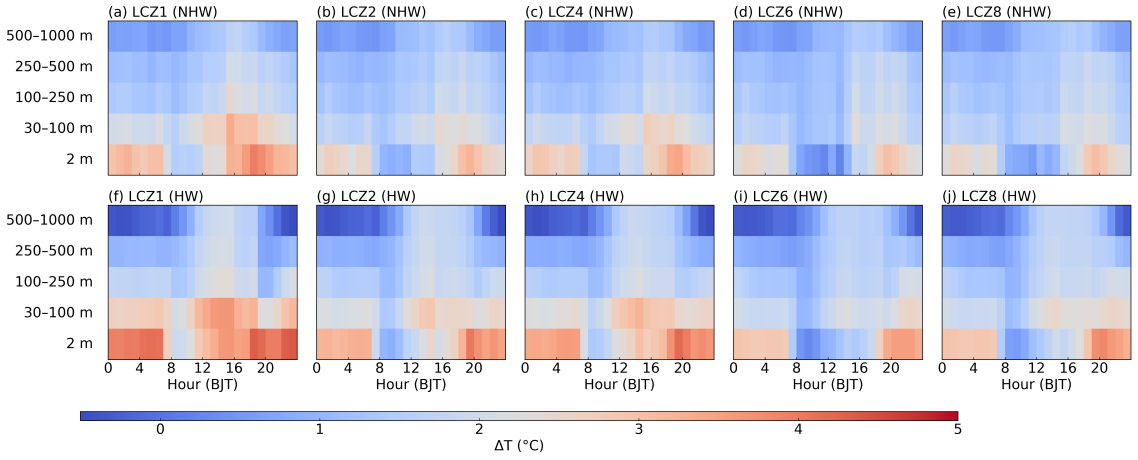

Figure S4. Vertical distribution of Layer ΔT between each LCZ and the rural reference area for (top row) the NHW period and (bottom row) the HW period: (a, f) LCZ 1; (b, g) LCZ 2; (c, h) LCZ 4; (d, i) LCZ 6; (e, j) LCZ 8.

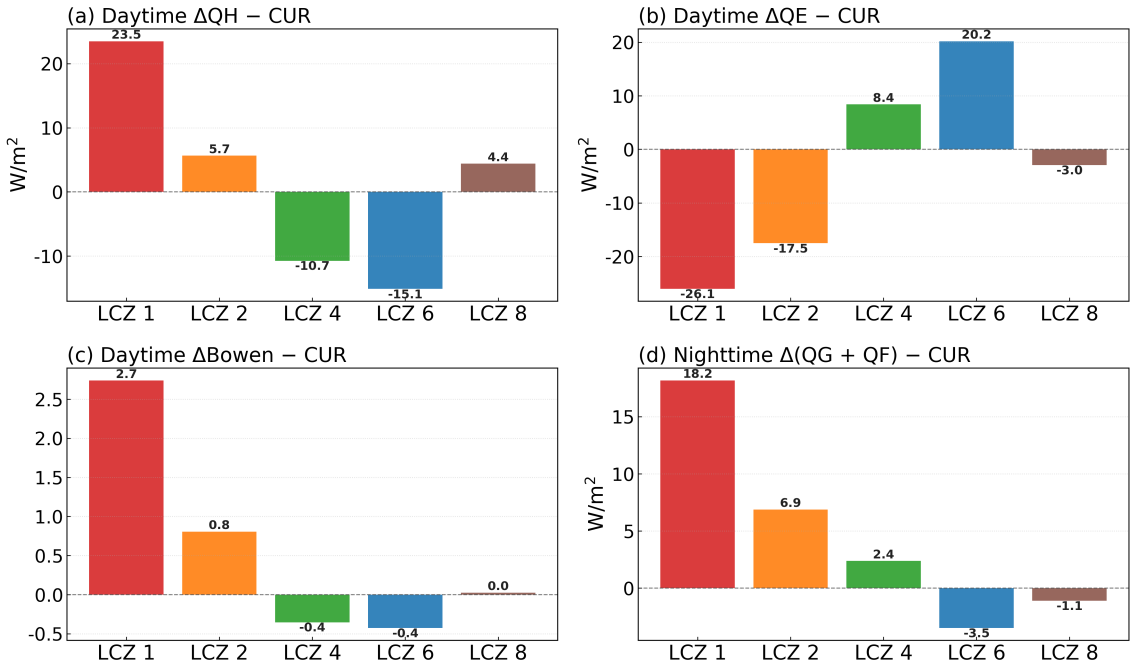

Figure S5. Deviations of HW - NHW differences in surface energy-balance components from the CUR-mean values for individual LCZs: (a) ΔQ_{H}; (b) ΔQ_{E}; (c) ΔBowen ratio; (d) $\Delta(Q_{\mathrm{G}} + Q_{\mathrm{F}})$.

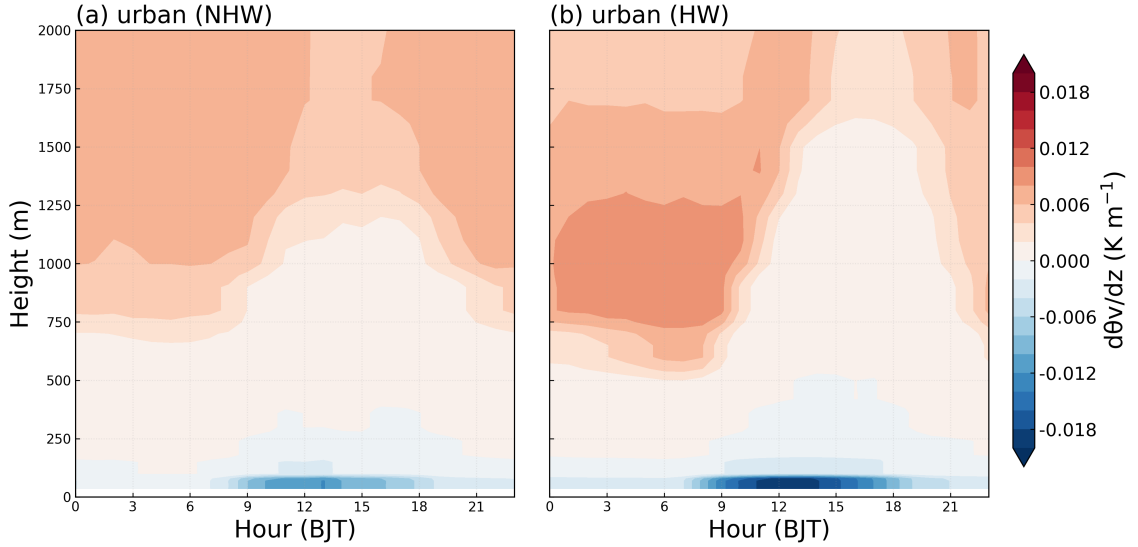

Figure S6. Vertical profile of potential temperature lapse rate ($\partial\theta/\partial$z) over the CUR during the periods NHW and HW1.

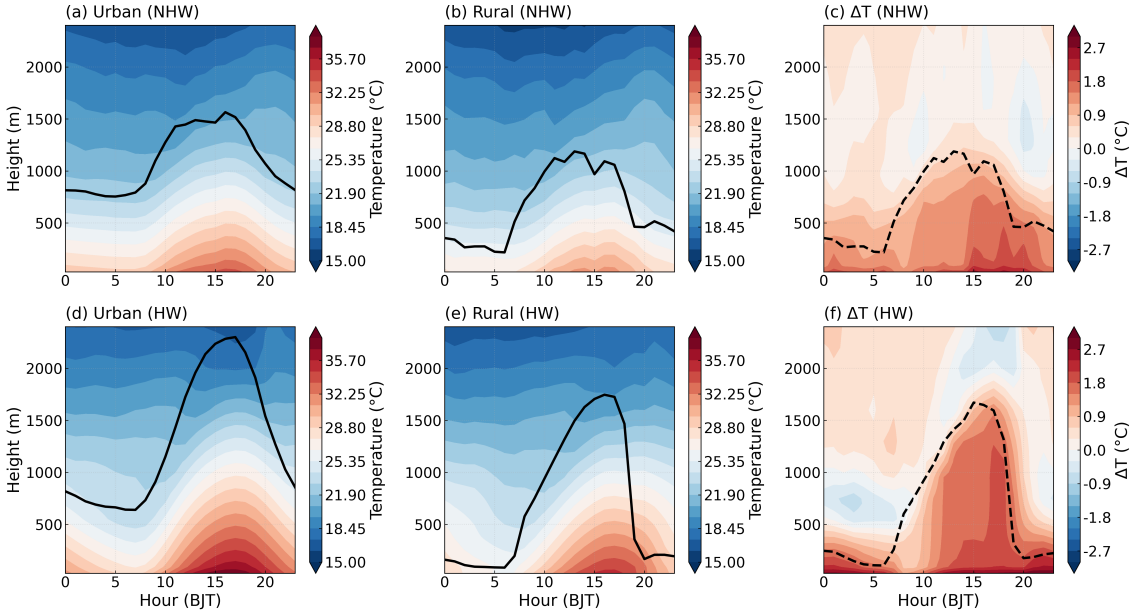

Figure S7. Vertical distributions of air temperature and the urban–rural air-temperature difference (ΔT) within 2500 m above ground over the urban and rural areas during the NHW and HW2 periods. The black solid lines in (a) and (d) indicate the urban PBLH; the black solid lines in (b) and (e) indicate the rural PBLH; the black dashed lines in (c) and (f) indicate the common dynamic PBL top used for the integration of BUHII during the NHW and HW2 periods.

Table S1. Indicators of thermal response and surface energy-balance response of the individual LCZs during the HW2 period compared to the NHW period. Δ denotes HW2 - NHW.

Indicator	LCZ 1	LCZ 2	LCZ 4	LCZ 6	LCZ 8
ΔCUHII daily mean (°C)	0.88	0.67	0.73	0.45	0.49
ΔCUHII nocturnal mean (°C)	1.27	1.16	1.15	0.98	1.00
30–100 m $\Delta\Delta T$ daily mean (°C)	0.67	0.54	0.57	0.36	0.39
30–100 m $\Delta\Delta T$ daytime mean (°C)	0.53	0.30	0.40	0.10	0.13
30–100 m $\Delta\Delta T$ nocturnal mean (°C)	0.81	0.77	0.75	0.63	0.65
ΔQ_{H} daytime mean ($\mathrm{W\,m^{-2}}$)	127.4	109.3	98.8	95.3	106.9
ΔQ_{E} daytime mean ($\mathrm{W\,m^{-2}}$)	−25.7	−19.0	1.1	9.7	−7.7
ΔBowen daytime mean	6.1	2.2	0.8	0.5	1.2
$\Delta(Q_{\mathrm{G}} + Q_{\mathrm{F}})$ nocturnal mean ($\mathrm{W\,m^{-2}}$)	44.8	33.6	29.3	22.8	25.8

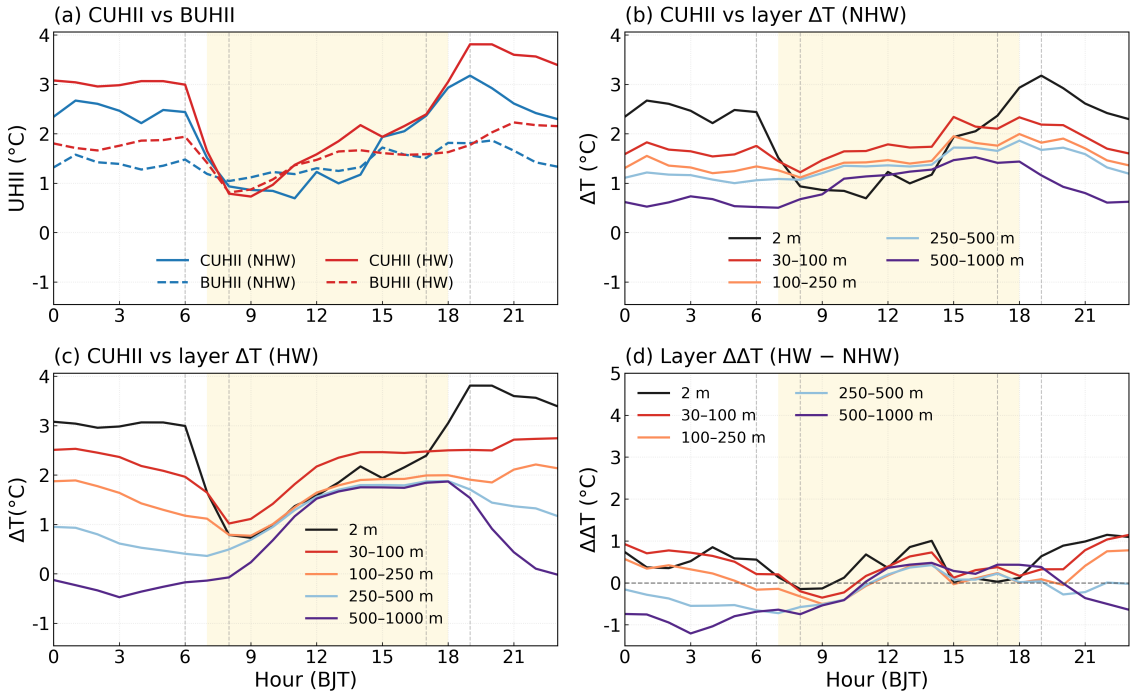

Figure S8. Diurnal cycles over the CUR. (a) CUHII (solid) and BUHII (dashed) during the NHW (blue) and HW2 (red) periods. (b) Layer ΔT at 2 m, 30–100 m, 100–250 m, 250–500 m, and 500–1000 m during the NHW period. (c) Same as (b) but for the HW2 period. (d) $\Delta\Delta T$ (HW2 - NHW) at the same five layers. Light-yellow shading indicates the daytime period (07:00–18:00 BJT); the hatched periods 06:00–08:00 BJT and 17:00–19:00 BJT indicate the morning and evening transitions, respectively.

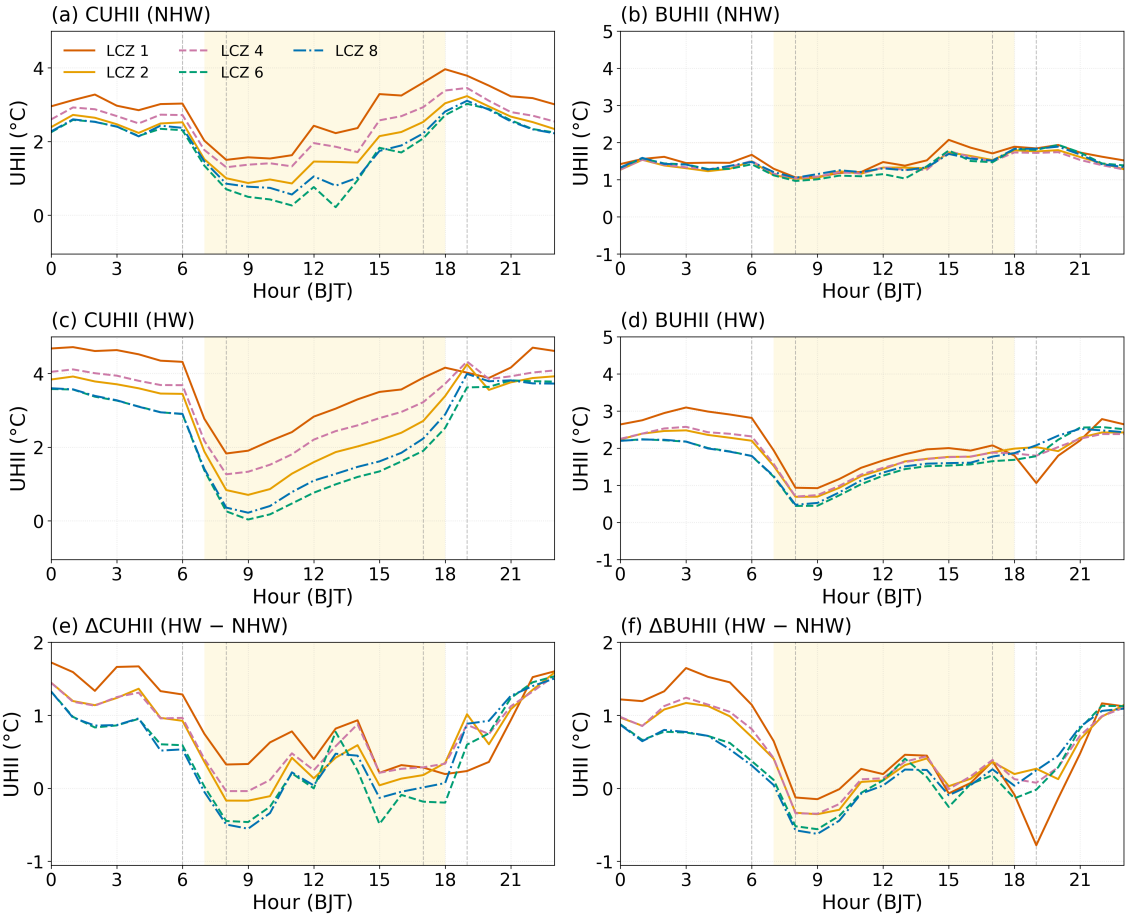

Figure S9. CUHII and BUHII diurnal cycles for the individual LCZs during the NHW and HW2 periods. (a) CUHII during the NHW period; (b) BUHII during the NHW period; (c) CUHII during the HW2 period; (d) BUHII during the HW2 period; (e) ΔCUHII (HW2 - NHW); (f) ΔBUHII (HW2 - NHW). Light-yellow shading indicates the daytime period (07:00–18:00 BJT); the hatched periods 06:00–08:00 BJT and 17:00–19:00 BJT indicate the morning and evening transitions, respectively.

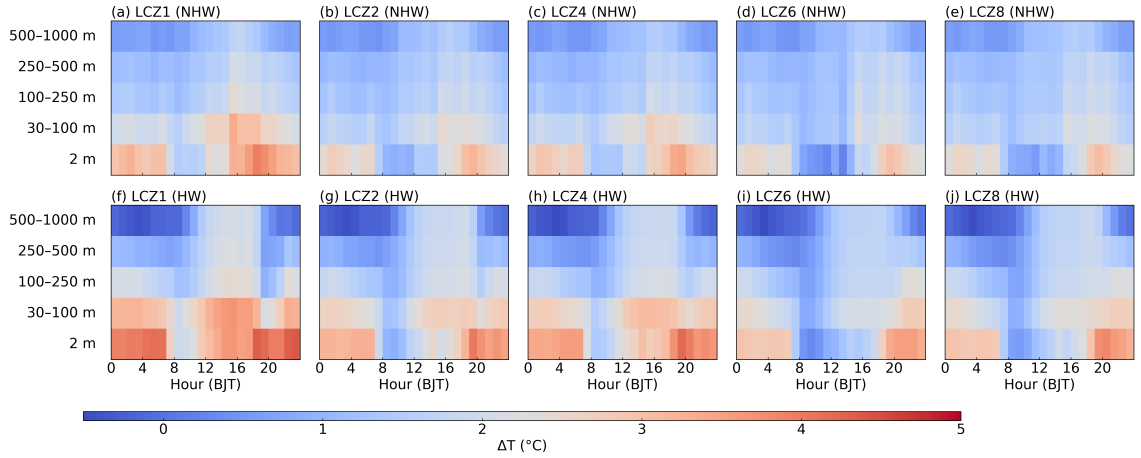

Figure S10. Vertical distribution of Layer ΔT between each LCZ and the rural reference area for (top row) the NHW period and (bottom row) the HW2 period: (a, f) LCZ 1; (b, g) LCZ 2; (c, h) LCZ 4; (d, i) LCZ 6; (e, j) LCZ 8.

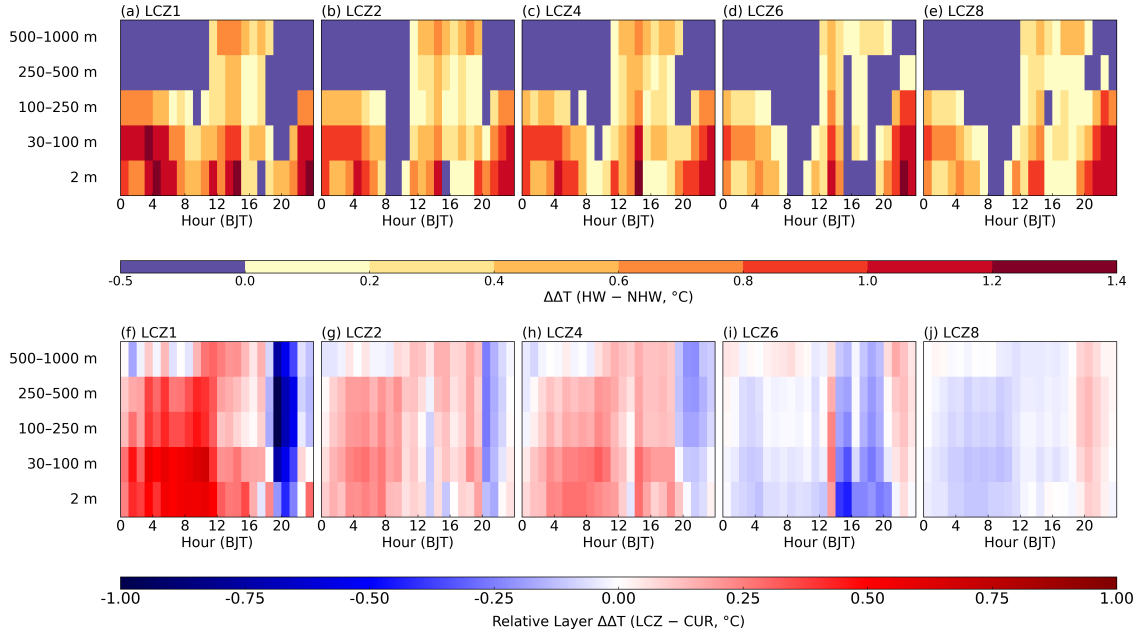

Figure S11. (a–e) Vertical distribution of Layer $\Delta\Delta T$ (HW2 - NHW) for LCZ 1, 2, 4, 6, and 8, respectively. (f–j) Deviations of each LCZ's Layer $\Delta\Delta T$ from the CUR-mean Layer $\Delta\Delta T$, in the same order as (a–e). Note that (a–e) and (f–j) use different colour scales.

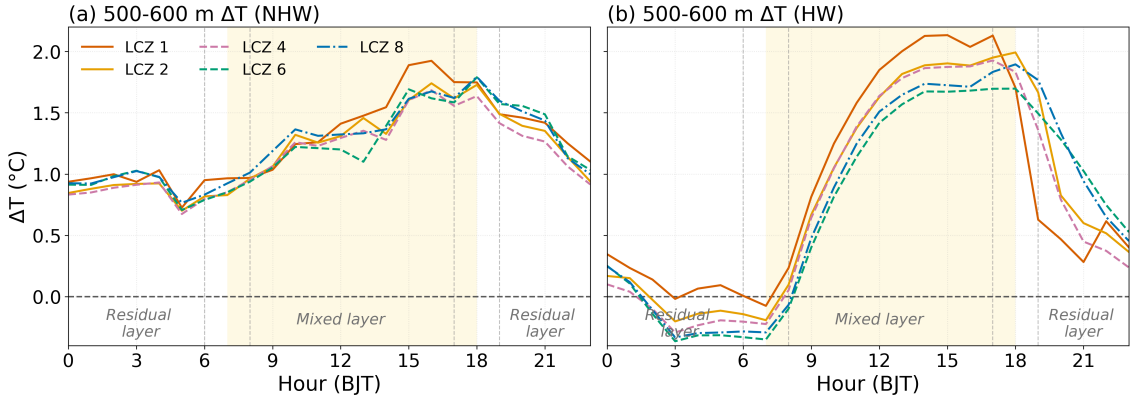

Figure S12. Diurnal cycles of ΔT at 500–600 m for individual LCZs during (a) the NHW period and (b) the HW2 period.

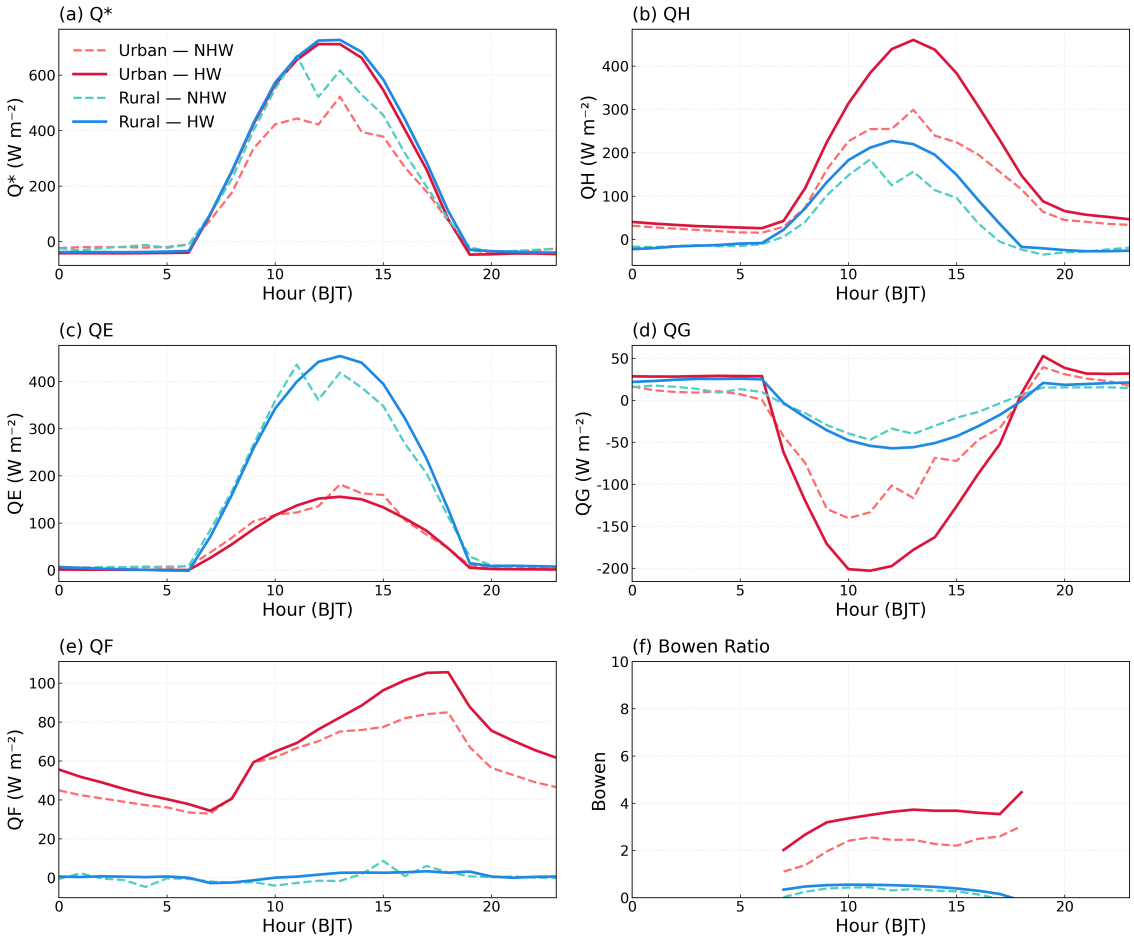

Figure S13. Diurnal cycles of the components of the surface energy-balance over the urban (red) and rural (blue) areas during the NHW (dashed) and HW2 (solid) periods: (a) net radiation Q^*; (b) sensible heat flux Q_{H}; (c) latent heat flux Q_{E}; (d) ground heat flux Q_{G}; (e) anthropogenic heat flux Q_{F} (estimated as a residual); and (f) Bowen ratio, calculated only when $Q^* > 0$.

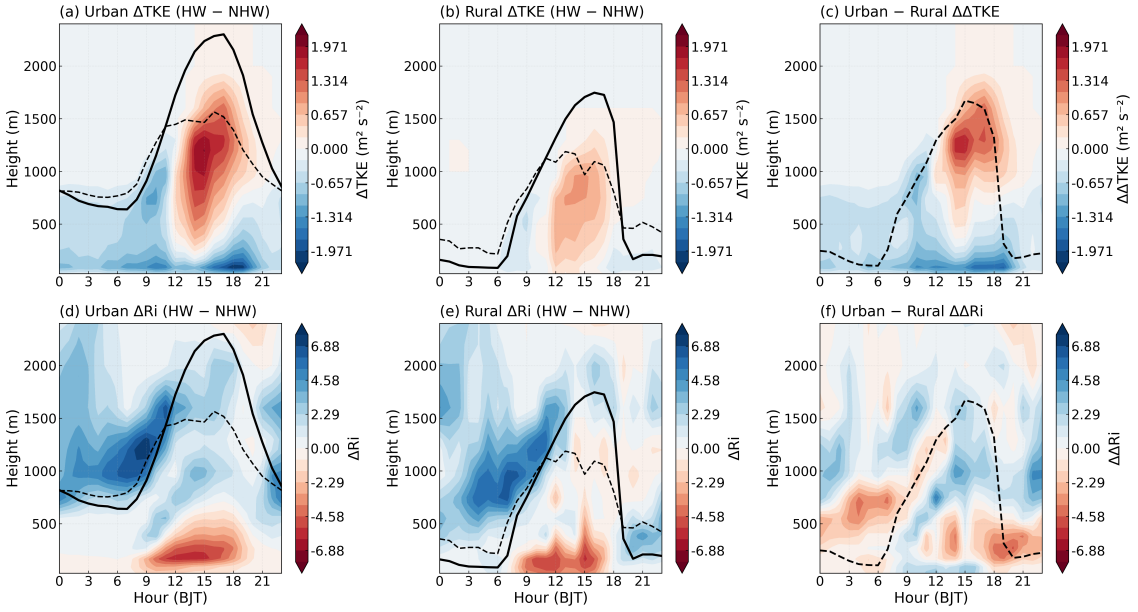

Figure S14. Vertical distributions of ΔTKE (HW2 - NHW; top row) and ΔRi (HW2 - NHW; bottom row): (a, d) over the urban area; (b, e) over the rural reference area; and (c, f) the urban–rural difference (ΔΔTKE and ΔΔRi). The black solid and dashed lines in (a) and (d) denote the urban PBLH during the HW2 and NHW periods, respectively; those in (b) and (e) denote the rural PBLH during the HW2 and NHW periods, respectively; and the black dashed lines in (c) and (f) denote the common dynamic PBL top H_c(t) during the HW2 period.

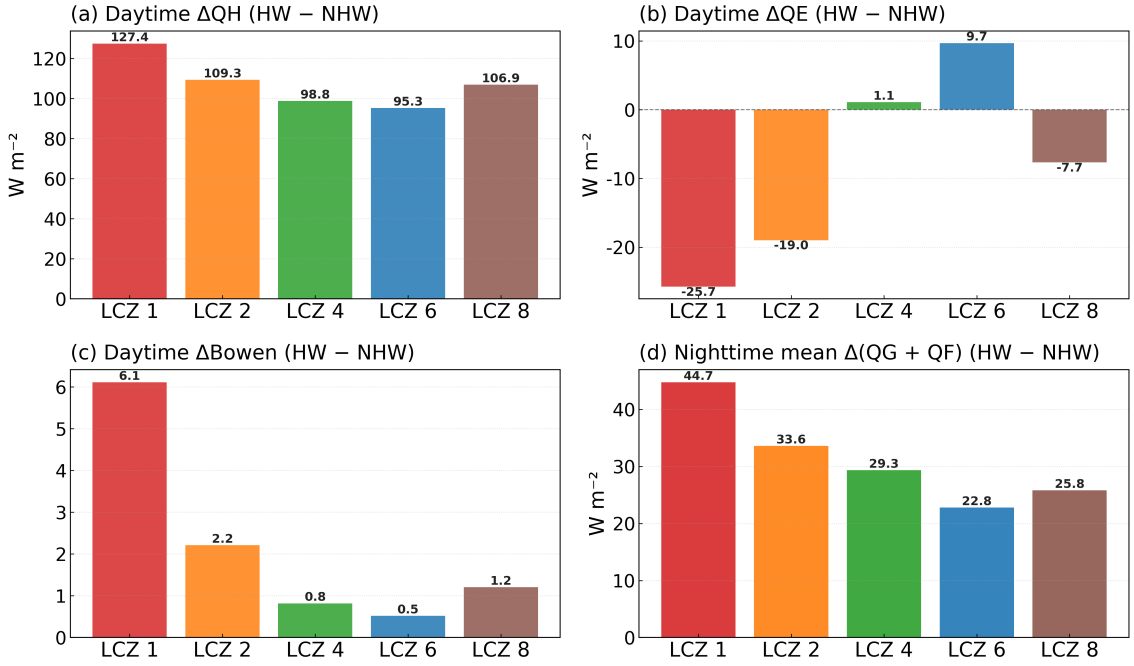

Figure S15. HW2 - NHW differences in surface energy-balance indicators for the individual LCZs: (a) daytime mean ΔQ_{H}; (b) daytime mean ΔQ_{E}; (c) daytime mean ΔBowen ratio; and (d) mean nocturnal $\Delta(Q_{\mathrm{G}} + Q_{\mathrm{F}})$. The numerical values are annotated on each bar.

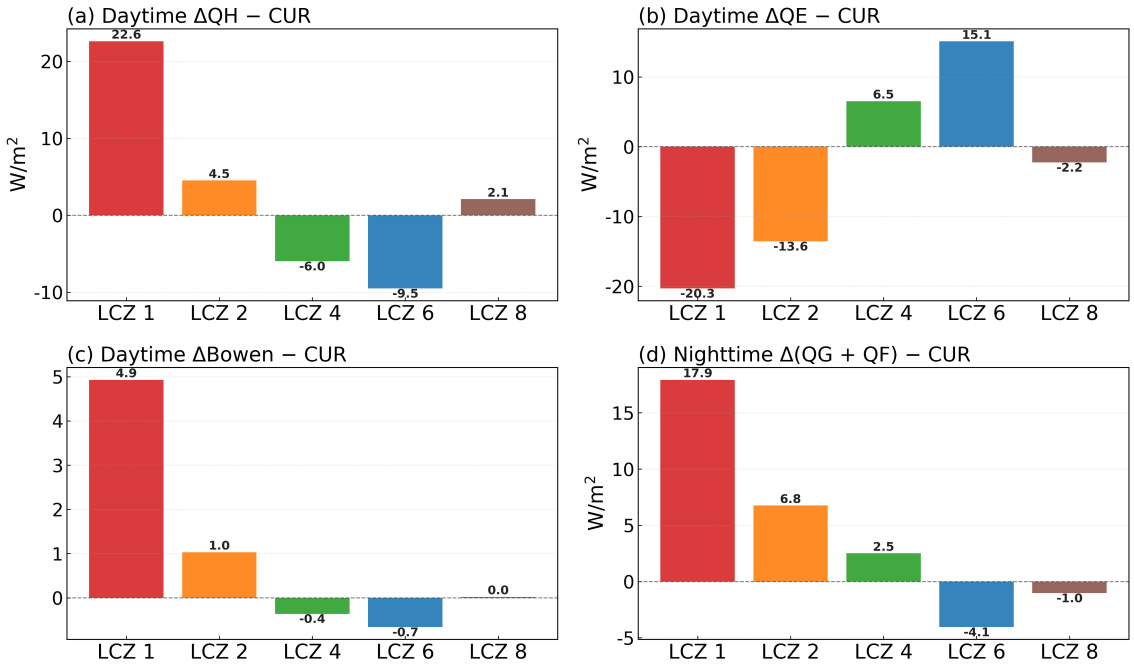

Figure S16. Deviations of the HW2 - NHW differences in the surface energy-balance components of the mean values of the CUR for the individual LCZs: (a) ΔQ_{H}; (b) ΔQ_{E}; (c) ΔBowen ratio; (d) $\Delta(Q_{\mathrm{G}} + Q_{\mathrm{F}})$.

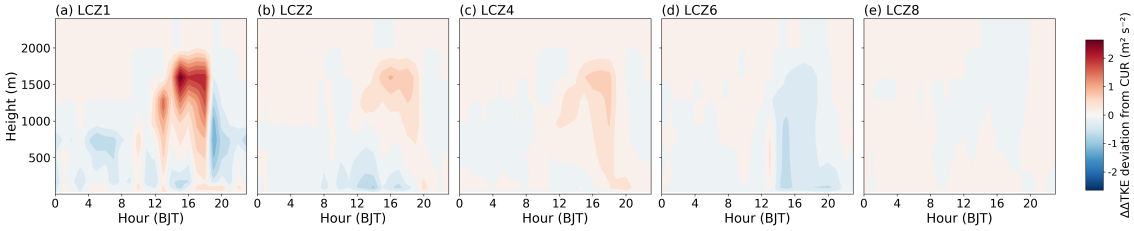

Figure S17. Vertical distributions of ΔΔTKE, defined here as the deviation of each LCZ's HW2–NHW TKE response from the CUR-mean response, for (a) LCZ 1, (b) LCZ 2, (c) LCZ 4, (d) LCZ 6, and (e) LCZ 8.

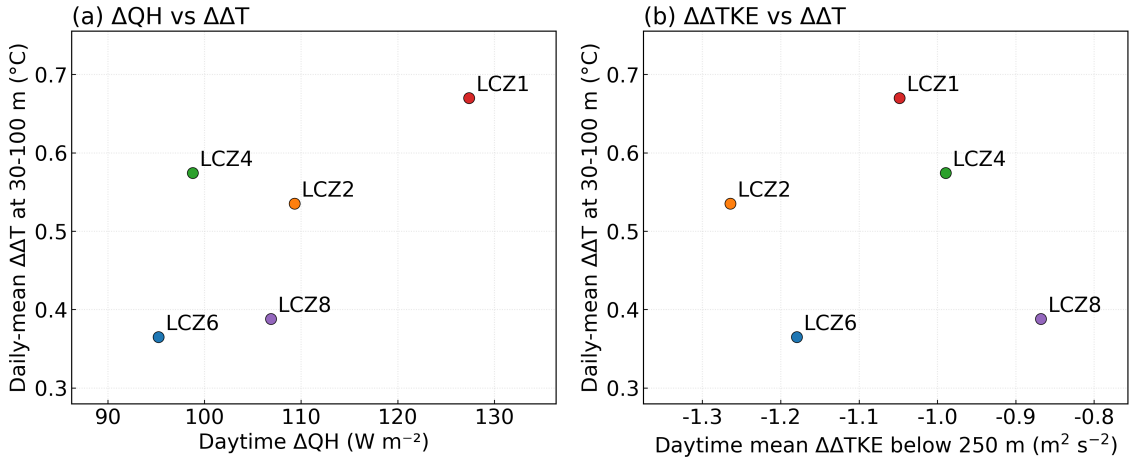

Figure S18. Scatter plots of the daily mean $\Delta\Delta T$ in the 30–100 m layer for individual LCZs against (a) the daytime mean ΔQ_{H}, and (b) the daytime mean $\Delta\Delta$TKE below 250 m.

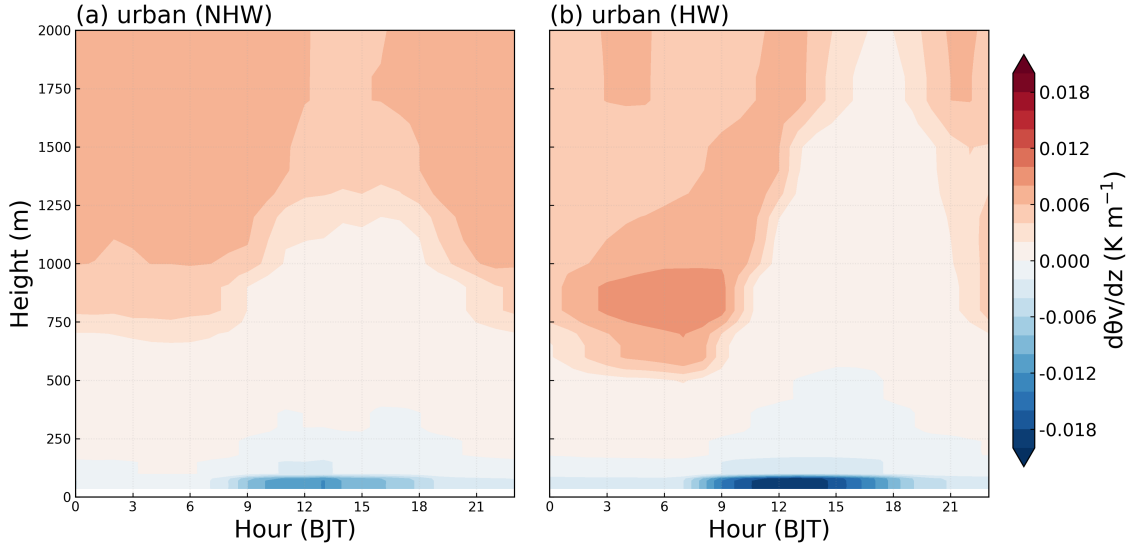

Figure S19. Vertical profile of the potential temperature lapse rate ($\partial\theta/\partial$z) over the CUR during the periods NHW and HW2.

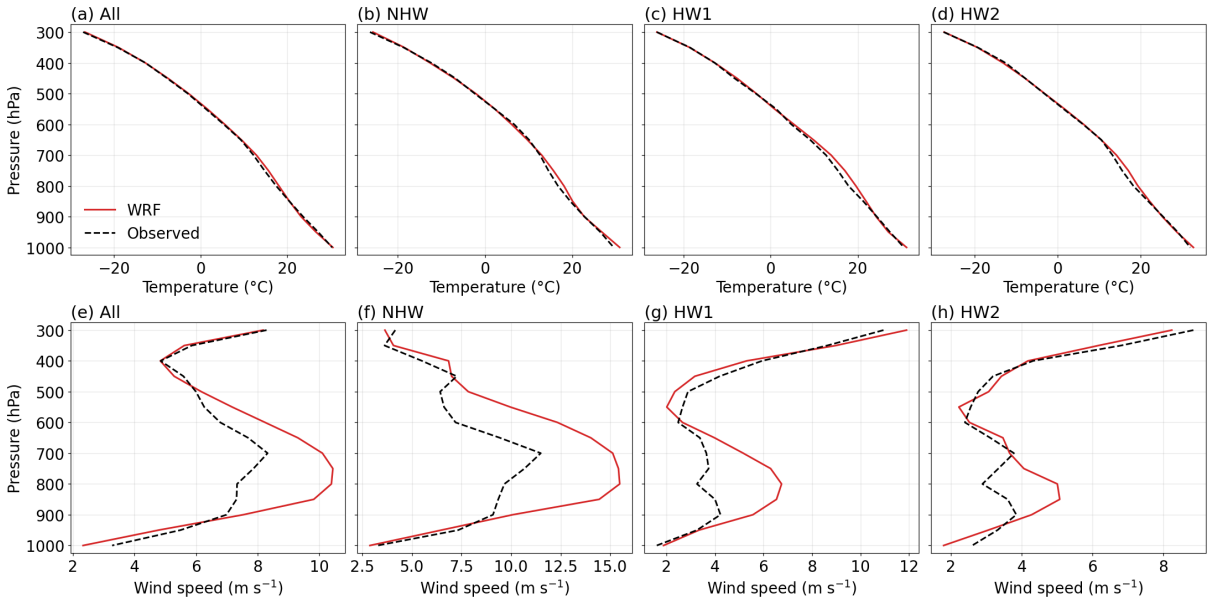

Figure S20. Comparison of WRF and Qingyuan IGRA radiosonde profiles for (columns) all matched soundings during 6–29 July 2020, the NHW period, HW1, and HW2. The top row shows temperature and the bottom row wind speed. WRF profiles are shown as red solid lines and observations as black dashed lines. Profiles were averaged on the common pressure levels 1000, 950, 900, 850, 800, 750, 700, 650, 600, 550, 500, 450, 400, 350, and 300 hPa.

Table S2. Statistical evaluation of WRF temperature (T), wind speed (WS), and wind direction (WD) against Qingyuan IGRA soundings at all matched levels with pressure ≥ 50 hPa, shown for the full evaluation period and the NHW, HW1, and HW2 periods. WD errors use circular statistics.

	T (°C)			WS (m s^{-1})			WD (°)	
Period	bias	MAE	RMSE	bias	MAE	RMSE	circular MAE	circular bias
All	0.07	1.06	1.46	0.87	2.55	3.39	29.8	−2.0
NHW	0.12	1.17	1.58	1.34	2.73	3.42	31.9	1.3
HW1	0.14	1.03	1.34	0.94	2.33	2.88	37.8	7.0
HW2	0.04	0.84	1.21	0.41	1.72	2.26	33.8	−18.4

Table S3. Statistical evaluation of WRF temperature (T), wind speed (WS), and wind direction (WD) against Qingyuan IGRA soundings across selected pressure layers for all matched soundings during 6–29 July 2020. WD errors use circular statistics.

	T (°C)			WS (m s^{-1})			WD (°)	
Pressure layer	bias	MAE	RMSE	bias	MAE	RMSE	circular MAE	circular bias
1000–850 hPa	−0.24	1.03	1.37	−0.15	1.85	2.56	28.4	1.5
850–700 hPa	0.54	1.06	1.38	2.60	2.85	3.41	33.0	−8.4
700–500 hPa	0.32	0.97	1.27	1.39	2.58	3.28	31.4	2.1
500–300 hPa	0.10	0.67	0.88	0.48	2.16	2.91	43.9	3.0